Research article

Lian Shen, Ludmila J. Prokopeva, Hongsheng Chen* and Alexander V. Kildishev*

Designing optimal nanofocusing with a gradient hyperlens

https://doi.org/10.1515/nanoph-2017-0054
Received May 17, 2017; accepted September 11, 2017

Abstract: We report the design of a high-throughput gradient hyperbolic lenslet built with real-life materials and capable of focusing a beam into a deep sub-wavelength spot of λ/23. This efficient design is achieved through high-order transformation optics and circular effective-medium theory (CEMT), which are used to engineer the radially varying anisotropic artificial material based on the thin alternating cylindrical metal and dielectric layers. The radial gradient of the effective anisotropic optical constants allows for matching the impedances at the input and output interfaces, drastically improving the throughput of the lenslet. However, it is the use of the zeroth-order CEMT that enables the practical realization of a gradient hyperlens with realistic materials. To illustrate the importance of using the CEMT versus the conventional planar effective-medium theory (PEMT) for cylindrical anisotropic systems, such as our hyperlens, both the CEMT and PEMT are adopted to design gradient hyperlenses with the same materials and order of elemental layers. The CEMT- and PEMT-based designs show similar performance if the number of metal-dielectric binary layers is sufficiently large (9+ pairs) and if the layers are sufficiently thin. However, for the manufacturable lenses with realistic numbers of layers (e.g. five pairs) and thicknesses, the performance of the CEMT design continues to be practical, whereas the PEMT-based design stops working altogether. The accurate design of transformation optics-based layered cylindrical devices enabled by CEMT allow for a new class of robustly manufacturable nanophotonic systems, even with relatively thick layers of real-life materials.

Keywords: non-imaging optics; nanofocusing; effective-medium theory; transformation optics; hyperlens.

***Corresponding authors: Hongsheng Chen,** State Key Laboratory of Modern Optical Instrumentation, Zhejiang University, Hangzhou 310027, China; and The Electromagnetics Academy at Zhejiang University, Zhejiang University, Hangzhou 310027, China, e-mail: hansomchen@zju.edu.cn; and
Alexander V. Kildishev, Birck Nanotechnology Center and Purdue Quantum Center, School of Electrical and Computer Engineering, Purdue University, 1205 W State St, West Lafayette, IN 47907, USA, e-mail: kildishev@purdue.edu. http://orcid.org/0000-0002-8382-8422
Lian Shen: Birck Nanotechnology Center and Purdue Quantum Center, School of Electrical and Computer Engineering, Purdue University, 1205 W State St, West Lafayette, IN 47907, USA; State Key Laboratory of Modern Optical Instrumentation, Zhejiang University, Hangzhou 310027, China; and The Electromagnetics Academy at Zhejiang University, Zhejiang University, Hangzhou 310027, China
Ludmila J. Prokopeva: Birck Nanotechnology Center and Purdue Quantum Center, School of Electrical and Computer Engineering, Purdue University, 1205 W State St, West Lafayette, IN 47907, USA; and Novosibirsk State University, Novosibirsk, Russia

1 Introduction

Concentrating optical energy into the smallest possible volume for a given free-space wavelength λ is one of the primary goals of non-imaging nanofocusing devices. Nanofocusing [1] has been explored for sensing [2] and nonlinear optics [3–5] through engineered antennas [6–8] and waveguides [9, 10]. Another immediate application of nanofocusing is in the industrially viable development of deep sub-wavelength optical lithography [11, 12]. Extreme nanofocusing is now recognized as a scientifically interesting method of generating the intense sub-wavelength-confined optical fields. However, translating nanophotonic nanofocusing techniques beyond proof-of-principle concepts to technologically relevant implementations remains a challenge. Although various attempts have been made to address this challenge, most approaches sacrifice industrial scalability for the sake of core metrics, such as throughput and focusing performance.

Recently, with the advent of the hyperlenses [13–18] and the rapid development of the enhanced nanofabrication techniques, there has been a renewed interest in nanofocusing with hyperbolic media. In particular, a growing interest in utilizing the hyperlens techniques for optical lithography has emerged [19–23]. A hyperlens may be achieved through the fabrication of the concentric cylindrical binary metal-dielectric layers. The layered

anisotropic lenslets with dielectric constants having opposite signs in the radial and tangential directions can, in principle, support the propagating waves with arbitrarily high wavenumbers [13]. Given that the diffraction limit of conventional optics is related to the upper bound on the wavenumber of the propagating waves, a hyperlens, a metamaterial-based lens with hyperbolic dispersion [19–25], is not subject to this limit. Hence, it could be considered a promising nanofocusing design prototype for optical lithography and for other important applications.

Transformation optics (TO) is a systematic approach to constructing extreme photonic devices. This approach has already been used to optimize imaging devices and, when transferred to a ray optics framework, as a tool for designing omnidirectional light concentrators and absorbers [26]. A hyperlens with an impedance-matched single interface for super-resolution imaging has already been demonstrated [14]. However, it is not obvious whether this approach for imaging could be (i) successfully applied to a nanofocusing device, and (ii) further improved to enhance the throughput by matching impedances at both the input and output interfaces.

In the current paper, we report an approach for designing optimal nanofocusing with a high-throughput gradient hyperlens. The idealized gradient hyperlens (GHL) described in Section 2 focuses a beam into a deep sub-wavelength (about λ/23) spot with an output to input power throughput ratio of about 14. However, when this GHL is approximated with nine pairs of metal-dielectric layers, as described in Section 3, it gives comparable nanofocusing of λ/23 with a power throughput ratio of about 6. Such optimal performance is achieved via high-order transformation optics and a circular effective-medium theory (CEMT). These two techniques are adopted to engineer the radially varying the anisotropic artificial material based on the metal-dielectric bilayers, which are thin, alternating cylindrical metal and dielectric layers. The radial gradient of the effective anisotropic optical constants is designed using a high-order transformation optics approach [27]. Specifically, we use a cubic scaling transformation that makes matching the impedances at the input and output interfaces possible, thus providing a theoretical foundation for the significant throughput enhancement. However, it is the use of zeroth-order CEMT that allows us to implement the theory and enable the practical realization of the GHL designs with real-life metals and dielectrics.

To showcase the importance of CEMT (instead of a commonly adopted planar effective-medium theory, PEMT) for a layered anisotropic cylindrical system, such as our gradient hyperlens, both CEMT and PEMT are adopted in two hyperlens designs with the same materials and order of elemental layers. The CEMT- and PEMT-based designs show a similar performance if the number of metal-dielectric binary layers is sufficiently large (9+ bilayers) and hence the elemental layers are thin. However, for manufacturable lenses with a practical number of metal-dielectric bilayers (e.g. five pairs) and realistic thicknesses, the performance of the CEMT design continues to be acceptable, whereas the PEMT-based design exhibits a significant drop in performance. The initial prototypes of the layered transformation optics-based cylindrical devices enabled by CEMT allowed us to design a truncated half-cylinder lenslet with only five binary layers numerically optimized for manufacturabililty. As shown in Section 3, such a 440-nm radius device deposited on a substrate can provide a λ/13 spot with about 3.5 power throughput ratio. The proposed analysis and design techniques could mitigate the technical and complicated fabrication processes of hyperlenses. Furthermore, the proposed approach may be utilized to design nanophotonic structures for enhancing collection efficiency of single-photon sources and other quantum emitters.

2 Materials and methods

2.1 Nanofocusing with a higher-order transformation

We start with an analysis of how to simplify an ideal nanofocusing device designed via transformation optics. An ideal nanofocusing lens maps the field from its outer to inner interface in a controlled way. A trivial example of such a transformation is a very thin ring [27]. If we could transform this virtual ring into a physical domain with non-zero dimensions, preserving the field pattern at the boundaries, the resulting device would enable "ideal" nanofocusing (see Figure 1).

The scalar Helmholtz wave propagation equation is used to describe the system with cylindrical symmetry. For TM polarization, the magnetic field is expanded in a series and shown for an mth azimuthal Fourier mode, $h(\rho, \phi) = \sum h_m(\rho) \exp \imath m\phi$. Hence, the wave equation for the mth mode is reduced to

$$\varepsilon_\rho \rho^{-1} (\rho \varepsilon_\phi^{-1} h_m')' + [k^2 \varepsilon_\rho \mu_z - (m/\rho)^2] h_m = 0. \quad (1)$$

Here, the physical Cartesian coordinates (x, y, z) are defined through the cylindrical coordinates (ρ, ϕ, z) as $x = \rho\cos\phi$, $y = \rho\sin\phi$, and $z = z$; the prime corresponds to

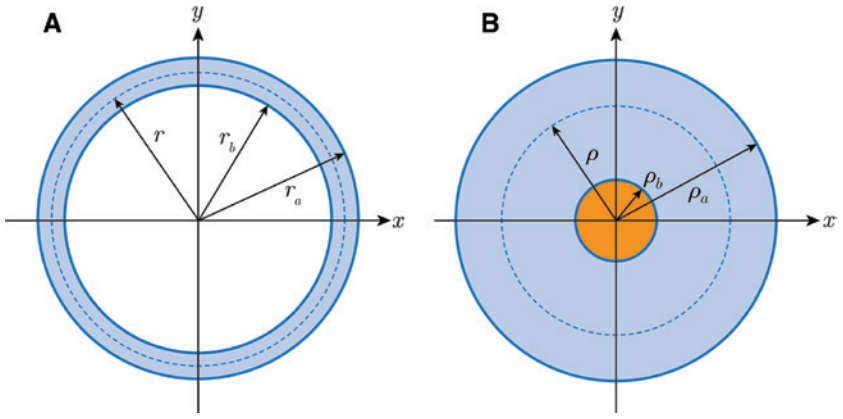

Figure 1: Transformations of concentric circular domains.
Mapping of a thin circular ring in panel (A), $r_b \le r \le r_a$, onto an expanded ring in panel (B), $\rho_b \le \rho \le \rho_a$.

the radial derivative $(\partial/\partial\rho)$; ε_ρ and ε_ϕ are the only non-zero diagonal components of the anisotropic permittivity tensor; and k is the wavenumber in free-space. Now we assume the coordinate transformation $\rho=\rho(r)$, shown in Figure 1, that maps a thin circular ring $r_b \le r \le r_a$ onto an expanded ring $\rho_b \le \rho \le \rho_a$. In this case, the external boundary, $r_a=\rho_a$, is shared by both domains. Given that $f'=r'f^{(r)}$ with $f^{(r)}=\partial/\partial r$, Eq. (1) yields

$$\left(\tilde{\varepsilon}_\rho\left(\frac{\rho}{r}\right)^2\right)r^{-1}(\tilde{\varepsilon}_\phi^{-1}(r')^2 r h_m^{(r)})^{(r)}+\left[k^2\left[\tilde{\varepsilon}_\rho\tilde{\mu}_z\left(\frac{\rho}{r}\right)^2\right]-\left(\frac{m}{r}\right)^2\right]h_m=0. \tag{2}$$

Matching this equation to the Helmholtz equation in vacuum gives the nonmagnetic material parameters expressed as

$$\tilde{\varepsilon}_\phi=(r')^2,\ \tilde{\varepsilon}_\rho=(r/\rho)^2,\ \tilde{\mu}_z=1, \tag{3}$$

with all the intermediate derivation steps being shown in the Supplementary Materials, Section S1.

In order to suppress reflection losses and improve the nanofocusing performance of our lens, impedance matching at both internal and external interfaces is critical. From Eq. (3), the impedance at both internal (output) and external (input) boundaries is given by

$$Z\big|_{\rho=\rho_{a,b}}=\sqrt{\tilde{\mu}_z/\tilde{\varepsilon}_\phi}\Big|_{\rho=\rho_{a,b}}=n_{a,b}^{-1}, \tag{4}$$

where n_a and n_b and are the refractive index of the outer and inner media, respectively. Following the conditions for the transformation derived, we ansatz a cubic transformation function as

$$r(\rho)=\alpha\rho^3+\beta\rho^2+\chi\rho+\delta, \tag{5}$$

satisfying the following system that defines the required coefficients given by

$$\begin{pmatrix}3\rho_a^2 & 2\rho_a & 1 & 0\\ 3\rho_b^2 & 2\rho_b & 1 & 0\\ \rho_a^3 & \rho_a^2 & \rho_a & 1\\ \rho_b^3 & \rho_b^2 & \rho_b & 1\end{pmatrix}\begin{pmatrix}\alpha\\ \beta\\ \chi\\ \delta\end{pmatrix}=\begin{pmatrix}n_a\\ n_b\\ r_a\\ r_b\end{pmatrix}. \tag{6}$$

The proposed transformation (5–6) (i) satisfies the required boundary conditions at $\rho=\rho_{a,b}$, and (ii) yields ideal focusing once the nonmagnetic constitutive parameters (3) are utilized.

The extreme anisotropy required for the transformation, as derived in the expressions of constitutive parameters (3), remains the most challenging limitation for lens construction, which also prevents its practical implementation. In particular, our nanofocusing device may require very large and positive ε_ρ, which would be difficult to implement with existing naturally occurring materials. To relax this limitation, we introduce an azimuthal transformation $\phi=\phi(f)$ that switches ε_ρ to become negative. Assuming that $s>0$, $(s\in\mathbb{R})$, we consider the azimuthal transformation as $f^{(\phi)}=(-s)^{-1/2}$. Upon transformation, Eq. (2) may be rewritten as

$$\left(\tilde{\varepsilon}_\rho\frac{1}{-s}\left(\frac{\rho}{r}\right)^2\right)r^{-1}(\tilde{\varepsilon}_\phi^{-1}(r')^2 r h_m^{(r)})^{(r)}+\left[k^2\left[\tilde{\varepsilon}_\rho\tilde{\mu}_z\frac{1}{-s}\left(\frac{\rho}{r}\right)^2\right]-(m/r)^2\right]h_m=0, \tag{7}$$

with a reduced set of nonmagnetic parameters given by

$$\tilde{\varepsilon}_\phi=(r')^2,\ \tilde{\varepsilon}_\rho=-s(r/\rho)^2,\ \tilde{\mu}_z=1. \tag{8}$$

with all the intermediate derivation steps being discussed in the Supplementary Materials, Section S1. One thing to

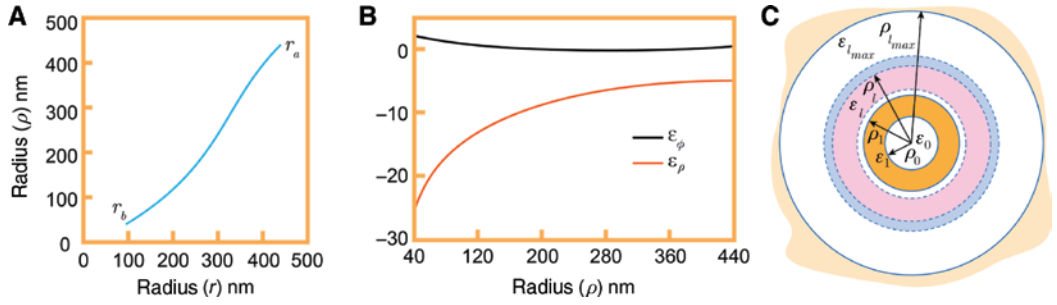

Figure 2: Details of the transformation optics design.
(A) Schematic figure of the transformation function for $r_b = 95$ nm. (B) Anisotropic material properties (dielectric function) of the ideal nanofocusing device. (C) Schematic configuration of an approximate layered system.

note is that parameter s is unconstrained. As it defines the dispersion operating point, we may choose the parameter to match the operation point with the dispersive dielectric function of an available real-life metal used in our design. A detailed discussion of this important point is done in the Supplementary Materials, Section S6.

We design a nanofocusing lenslet operating in air, $n_a = 1$, with $\rho_a = 440$ nm and $\rho_b = 40$ nm. The refractive index of the inner medium is $n_b = 1.64$, which is close to a typical refractive index of the optical lithography photoresist. For this optical lithography example, we propose a transformation function with practically realizable values of $r_b = 95$ nm and $s = 4.5$. Figure 2A depicts the cubic transformation function, and Figure 2B shows the required anisotropic material properties of the nanofocusing device. Therefore, we come to the "ideal" constitutive parameters based on radial and azimuthal scaling transformations by considering both the focusing performance and the practical realization.

2.2 Layered systems: the CEMT and PEMT designs

The practical implementation of the proposed nanofocusing device would require an approximation technique, wherein the theoretical smooth distribution of radially dependent anisotropic material properties (see Figure 2B) is substituted with a number of manufacturable layers, as shown in Figure 2C. In this section, we analyze a nanofocusing device consisting of two distinct homogeneous materials (i.e. a binary metal-dielectric composite).

Generally, for implementing gradient optical devices, a smooth ideal distribution of optical properties is approximated by a few layers of homogeneous materials. To accomplish this distribution, the sub-wavelength thin layers of the dispersive and non-dispersive homogeneous materials are carefully chosen and arranged. The effective material properties of a binary-phase cylindrical structure can be obtained from the quasistatic approximations [23]

$$\begin{aligned} \varepsilon_{\rho,l}^{-1} \ln\frac{\rho_{l+2}}{\rho_l} &= \varepsilon_l^{-1} \ln\frac{\rho_{l+1}}{\rho_l} + \varepsilon_{l+1}^{-1} \ln\frac{\rho_{l+2}}{\rho_{l+1}} \\ \varepsilon_{\phi,l} \ln\frac{\rho_{l+2}}{\rho_l} &= \varepsilon_l \ln\frac{\rho_{l+1}}{\rho_l} + \varepsilon_{l+1} \ln\frac{\rho_{l+2}}{\rho_{l+1}} \end{aligned}, \tag{9}$$

which comprise the zeroth-order CEMT. Given that $\ln(1+x) \approx x + O(x^2)$, then for very thin layers, the CEMT equations (9) degenerate into the familiar expressions for the conventional planar effective-medium theory (PEMT) [23]. These equations are given by

$$\begin{aligned} \varepsilon_{\rho,l}^{-1} &= \varepsilon_l^{-1} \frac{\rho_{l+1}-\rho_l}{\rho_{l+2}-\rho_l} + \varepsilon_{l+1}^{-1} \frac{\rho_{l+2}-\rho_{l+1}}{\rho_{l+2}-\rho_l} \\ \varepsilon_{\phi,l} &= \varepsilon_l \frac{\rho_{l+1}-\rho_l}{\rho_{l+2}-\rho_l} + \varepsilon_{l+1} \frac{\rho_{l+2}-\rho_{l+1}}{\rho_{l+2}-\rho_l} \end{aligned}. \tag{10}$$

These two dielectric functions, presented in Eqs. (9) and (10), can be treated as the design rules for the cylindrical nanofocusing device. However, it is essential to understand which of these two, PEMT or CEMT, provides superior nanofocusing performance. One of the goals of Section 3 is to present and discuss the results of this comparison. An illuminating way to analyze the concentric cylindrical binary metal-dielectric layers via a conformal mapping transformation is shown in the Supplementary Materials, Section S4. The Section also provides the relations of the radii of individual layers between the PEMT- and CEMT-based designs.

3 Results and discussion

To demonstrate the focal performance of the design using the derived high-order transformation, we first

conduct field-mapping simulations using Fourier modal semi-analytical method. We choose an optical lithography relevant illumination wavelength of 365 nm. The geometry and material properties are the same as those shown in Section 2, specifically, Figure 2A and B, respectively. In this simulation, a TM-polarized Gaussian beam with a waist of $w=\lambda$ is incident from the top boundary. The beam focus is located at the origin $x_0=0$, $y_0=0$. For the "ideal" design, the irradiance and the *H*-field of the Gaussian beam is depicted in Figure 3A and B, respectively. The details on the Gaussian beam illumination are presented in the Supplementary Materials, Section S3. The FEM simulations are also compared with the exact analytical expansion solutions of the wave equation, as shown in the Supplementary Materials, Section S7, Figure S4. Figure 3C depicts the plot of the normalized irradiance for the high-order transformation design. The output port is located at $\rho=(\rho_b-1)$. The output irradiance here is normalized with respect to the input power of the Gaussian beam incident on the outer boundary. From the plot, we can observe that the cubic transformation yields excellent nanofocusing performance: the full-width-at-half-maximum (FWHM) of the central peak is about 16 nm (about λ/23) and the power throughput is about 14 times higher than the input power.

The materials used to approximate the continuous radius-dependent anisotropic permittivity (see Figure 2B) with discrete pairs of binary metal-dielectric layers are listed in Table 1 [28, 29]. The radii of the individual layers for the PEMT- and CEMT-based designs are shown in the Supplementary Materials, Section S5, Tables S1 and S2.

Both the simulated irradiance and *H*-field of the nanofocusing device with nine pairs of binary metal-dielectric layers at $\lambda=365$ nm are depicted in Figure 4. The PEMT (see Figure 4A–C) and CEMT (see Figure 4D–F) designs are tested. Additionally, we use the exact expansion solution of the wave equation to validate the simulation results,

Table 1: Material permittivity.

Ag	SiC	Si_3N_4	Al_2O_3	Air	Photoresist
$-2.5+0.23i$	7.9	4.37	3.07	1	$(1.64)^2$

as shown in the Supplementary Materials, Section S7, Figure S5. Both the PEMT- and CEMT-based designs exhibit similar focusing performance, due to the large number of layers and the slight variation of the layer thicknesses. The probes are taken to be the same as in Figure 3C. From the line profiles at the probes shown in Figure 4C and F, both designs are capable of creating a focused hotspot at the output boundary. The nanofocusing performance is comparable to the ideal case of Figure 3. Specifically, the FWHM is almost the same as in Figure 3C, which means that back reflection at the interface of each layer does not affect the focusing performance significantly. However, the reflection losses decrease the power throughput as the relative peak power for the PEMT design is decreased to about 5.5× the input power, whereas it is about 6× for the CEMT design in comparison with 14× for the ideal case. Therefore, even in the case of a larger number of layers and smaller thickness differences, the CEMT design still exhibit superior focusing performance compared with the PEMT design.

The performance gap between the PEMT- and CEMT-based designs becomes significantly more substantial as the number of layers decreases. After reducing the number of layers to five pairs, as depicted in Figure 5, the CEMT design (see Figure 5D–F) continues to perform well and confine light. The FWHM of the central peak widens to 32.5 nm (about λ/11) and the power throughput is about 3.7 times higher than the input power. However, for the PEMT design with five paired layers (see Figure 5A–C) the peak vanishes and the output power is much lower than the input power. We also use the expansion solution of

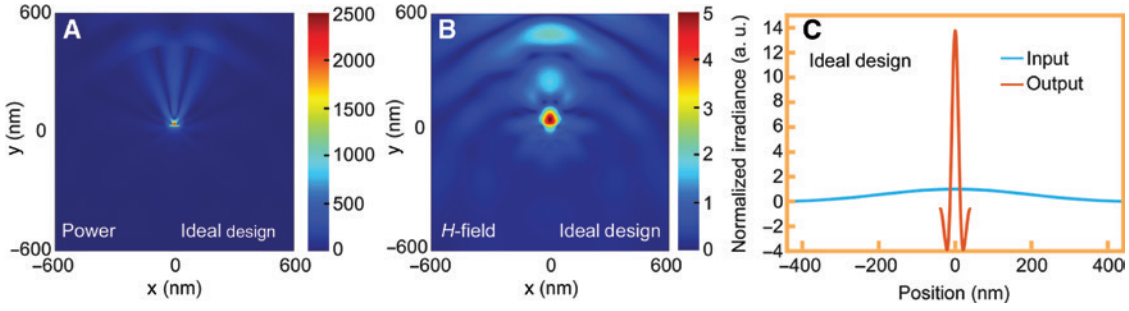

Figure 3: Full-wave field-mapping simulation of the "ideal" nanofocusing device.
(A) Simulated irradiances and (B) *H*-field magnitude at $\lambda=365$ nm generated by the exact non-paraxial Gaussian beam with a waist of $w=\lambda$. (C) Plot of the normalized irradiance for the "ideal" design.

the wave equation to verify these simulation results, as shown in the Supplementary Materials, Section S7, Figure S6. Additionally, the cases for six and seven pairs and the analysis of sensitivity to fabrication errors are discussed in the Supplementary Materials, Section S8 and Section S9, respectively.

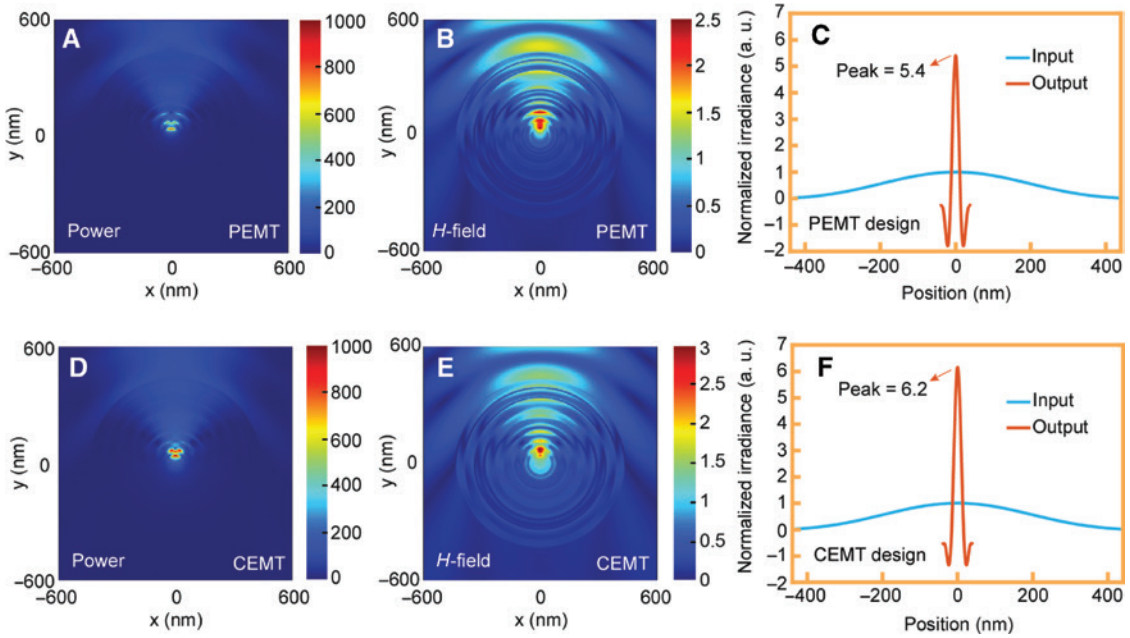

Figure 4: Full-wave field-mapping simulation of the nanofocusing device with nine pairs of binary metal-dielectric layers. (A–C) PEMT or (D–F) CEMT is used for two distinct designs. (A, D) Simulated irradiances and (B, E) *H*-field magnitude at $\lambda = 365$ nm generated by the exact non-paraxial Gaussian TM beam with a waist of $w = \lambda$. (C, F) Plots of the normalized irradiance for the nanofocusing device with nine pairs of binary metal-dielectric layers.

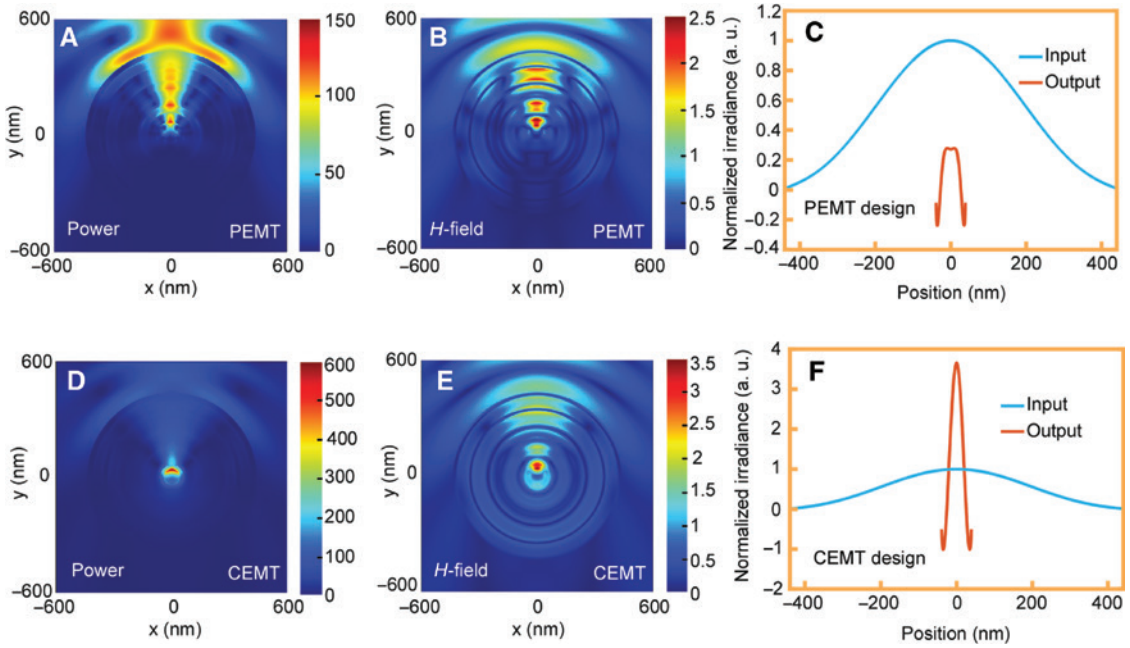

Figure 5: Full-wave field-mapping simulation of the nanofocusing device with five pairs of binary metal-dielectric layers. (A–C) PEMT or (D–F) CEMT is used for two distinct designs. (A, D) Simulated irradiances and (B, E) *H*-field magnitude at $\lambda = 365$ nm generated by the exact non-paraxial Gaussian beam with a waist of $w = \lambda$. (C, F) Plots of the normalized irradiance for the nanofocusing device with five pairs of binary metal-dielectric layers.

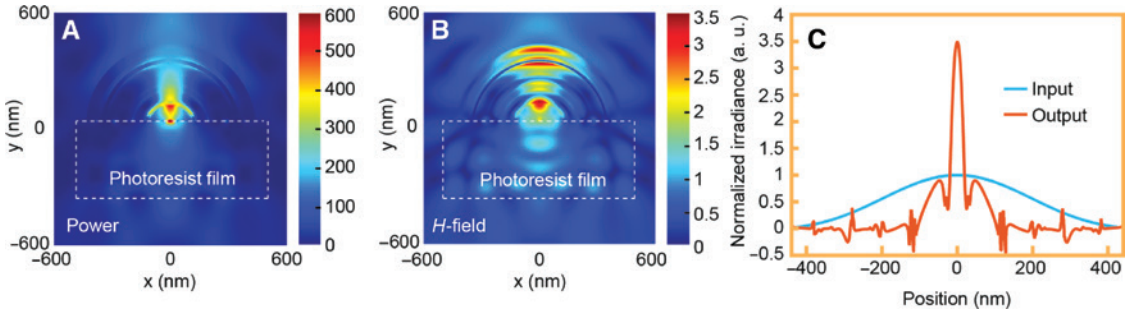

Figure 6: Optimization results.
(A) Simulated irradiances and (B) *H*-field magnitude at $\lambda = 365$ nm generated by exact non-paraxial Gaussian beam with a waist of $w = \lambda$. The substrate with a refractive index of 1.64 and a thickness of 400 nm are used. (C) Plot of the normalized irradiance for the nanofocusing device with five pairs of binary metal-dielectric layers.

Finally, we tested a structure designed specifically for manufacturability by truncating the cylinder with a flat output surface. The test was conducted by either depositing the structures on top of a flat substrate or embedding the structure in a host and then depositing a positive photoresist substrate film [21], as shown in Figure 6. In this case, truncating the cylinder affects the ideal nanofocusing and the approach based on the straightforward use of the cubic transformation concept fails to work. Nonetheless, it serves as an excellent initial guess for numerical optimization. Here, we take five pairs of bilayer metal-dielectric layers as an example and use the particle swarm optimization method to achieve good nanofocusing performance, as depicted in Figure 6. Note that when doing the optimization, we fix the same layer number, starting order, thickness of each pair, and dielectric permittivities. Following the optimization method, we obtain the thickness of each layer for five pairs of binary metal-dielectric layers, as shown in Table 2. Hence, the initial prototypes of layered TO-based cylindrical devices enabled by CEMT allowed us to design a truncated half-cylinder lenslet with only five binary layers, and numerically optimized for manufacturabililty. This 440-nm radius device deposited on a substrate focuses light into the λ/13 spot with a power throughput ratio of around 3.5, corresponding to 40% of the incident power transmitted into/absorbed by the photoresist substrate film. This performance is virtually the same as that of the fully cylindrical CEMT design despite only being a half shell. Additionally, a truncated design without photoresist film is discussed in the Supplementary Materials, Section S11.

In summary, our simulation results of the ideal gradient design and metal-dielectric layered designs demonstrate good focusing performance. The proposed higher-order TO CEMT design considerably outperforms a design using conventional PEMT with the same limited number of layers. Additionally, simulations demonstrate the validity of our CEMT design in a fabrication realistic setup – with the presence of the photo-resist layer and half cylinder form-factor (Figure 6). The proposed design procedure is general and can be utilized as an innovative approach to achieving robust nanofocusing.

Table 2: Five-pair design optimization.

Material	Thickness (nm)	
Ag	δ_1	13
Si_3N_4	δ_2	67
Ag	δ_3	16
Al_2O_3	δ_4	64
Ag	δ_5	35
Si_3N_4	δ_6	45
Ag	δ_7	58
SiC	δ_8	22
Ag	δ_9	24
SiC	δ_{10}	56

4 Conclusions

Generally, the layout densities of on-chip photonic circuits are restricted by the weak nature of the nonlinear optical interactions required for the all-optical signal processing. The capability to focus optical signals far below the vacuum wavelength using the plasmonics provides a route to enhance the weak optical nonlinearity in natural materials [30] when short interaction lengths are required. Additionally, the hybrid plasmonic waveguides [31, 32] are perhaps one of the most popular nanofocusing approaches to achieve integration with silicon photonics. Finally, in addition to waveguides [9, 10], other non-imaging nanofocusing devices, such as engineered antennas [6–8] and

metasurfaces, have also been actively explored for sensing [2], nonlinear optics [3–5], and optical lithography [11, 12]. TO offers a systematic approach to constructing extreme photonic devices. The approach has already been probed for optimizing non-imaging ray optics devices, including omnidirectional light concentrators and absorbers [26]. Moreover, a hyperlens with an impedance-matched single interface for super-resolution imaging has already been demonstrated [14]. In the current paper, we proposed an alternative method for nanofocusing with high-order TO, thus providing impedance-matching at the input and output interfaces, which could easily be propelled beyond proof-of-principle to technologically relevant implementation.

Furthermore, we prove in this paper, that a newly developed high-order TO can be successfully applied to a line of nanofocusing devices by using CEMT; this approach can even be further improved to enhance the throughput by matching impedances at both the input and output interfaces. In short, using the formalism of high-order transformation optics, we generalize the concept of an impedance-matched nanofocusing device and demonstrate how the reflection losses at both the interfaces of the nanofocusing lenslet can be completely suppressed. This approach eliminates the undesired scattering within the limit of geometric optics and thus improves device efficiency, yielding a deep sub-wavelength (about $\lambda/23$) spot with an output to input power throughput ratio of about 14. We also demonstrate that the proposed "ideal" nanofocusing device can be substituted by a lamellar structure using two distinct effective-medium theory zeroth-order approximations, namely, PEMT and CEMT. The semi-analytical simulations of the ideal and lamellar devices, which are illuminated with the Gaussian beam, indicate that the CEMT design demonstrates superior focusing performance and throughput versus the PEMT design for the same number and starting order of layers. Moreover, the conventional PEMT fails to adequately approximate the optical properties of the cylindrical structure in few-layer setups and provide nanofocusing in a realizable structure. From the conformal mapping point of view, we identify the genuinely curvilinear interfaces to be the cause of this disagreement. To correct this issue, we propose the CEMT design to realize a new nanofocusing device. By comparing with a conventional PEMT design, we find that the CEMT design improves the nanofocusing performance, particularly for the practical case of just a few binary metal-dielectric layers. Layered structures are commonly achieved by using the angled physical vapor deposition (see Supplementary Materials, Section S10). By adjusting the deposition angle and rotating the sample, this technique would allow for greater control over the thickness gradient from any angle along the curved surface, thus making it a promising method for fabricating a prototype device.

Our methodology, validated with numerically optimized truncated cylindrical lamellar structures, paves the way to designing practical nanofocusing systems and assessing the feasibility of few-layer structures compared with more complex multilayer counterparts for applications in transformative non-imaging applications.

Acknowledgments: L. S. and H. C. were sponsored by the National Natural Science Foundation of China (Grant Nos. 61625502, 61574127, and 61601408), the ZJNSF (Grant No. LY17F010008), the Top-Notch Young Talents Program of China, the Fundamental Research Funds for the Central Universities (Grant No. 2017XZZX008-06), and the Innovation Joint Research Center for Cyber-Physical-Society System. L. J. P. and A. V. K. were supported by the DARPA Optics and Imaging (EXTREME) program. The kind assistance of Samuel Peana in preparing the manuscript is greatly appreciated.

Conflict of interest statement: The authors declare no competing financial interest.

References

[1] Gramotnev DK, Bozhevolny SI. Nanofocusing of electromagnetic radiation. Nat Photonics 2013;8:13–22.
[2] Anker JN, Hall WP, Lyandres O, Shah NC, Zhao J, Van Duyne RP. Biosensing with plasmonic nanosensors. Nat Mater 2008;7:442–53.
[3] Park I-Y, Kim S, Choi J, et al. Plasmonic generation of ultrashort extreme-ultraviolet light pulses. Nat Photonics 2011;5:677–81.
[4] Sederber S, Elezzabi AY. Ponderomotive electron acceleration in a silicon-based nanoplasmonic waveguide. Phys Rev Lett 2014;113:167401.
[5] Xu K. Current-voltage characteristics and increase in the quantum efficiency of three-terminal gate and avalanche-based silicon LEDs. Appl Opt 2013;52:6669–75.
[6] Sidiropoulos TPH, Nielsen MP, Roschuk TR, Zayats AV, Maier SA, Oulton RF. Compact optical antenna coupler for silicon photonics characterized by third-harmonic generation. ACS Photonics 2014;1:912–6.
[7] Aouani H, Rahmani M, Navarro-Cía M, Maier SA. Third-harmonic-upconversion enhancement from a single semiconductor nanoparticle coupled to a plasmonic antenna. Nat Nanotechnol 2014;9:290–4.
[8] Kim S, Jin J, Kin Y-J, Park I-Y, Kim Y, Kim S-W. High-harmonic generation by resonant plasmon field enhancement. Nature 2008;453:757–60.
[9] Choo H, Kim M-K, Staffaroni M, et al. Nanofocusing in a metal-insulator-metal gap plasmon waveguide with a three-dimensional linear taper. Nat Photonics 2012;6:838–44.

[10] Stockman MI. Nanofocusing of optical energy in tapered plasmonic waveguides. Phys Rev Lett 2004;93: 137404.
[11] Srituravanich W, Pan L, Wang Y, Sun C, Bogy DB, Zhang X. Flying plasmonic lens in the near field for high-speed nanolithography. Nat Nanotechnol 2008;3:733–7.
[12] Wagner C, Harned N. EUV lithography: lithography gets extreme. Nat Photonics 2010;4:24–6.
[13] Jacob Z, Alekseyev LV, Narimanov E. Optical hyperlens: far-field imaging beyond the diffraction limit. Opt Express 2006;14:8247–56.
[14] Kildishev AV, Narimanov E. Impedance-matched hyperlens. Opt Lett 2007;32:3432–4.
[15] Salandrino A, Engheta N. Far-field subdiffraction optical microscopy using metamaterial crystals: theory and simulation. Phys Rev B 2006;74:075103.
[16] Liu Z, Lee H, Xiong Y, Sun C, Zhang X. Far-field optical hyperlens magnifying sub-diffraction-limited objects. Science 2007;315:1686.
[17] Lu D, Liu Z. Hyperlenses and metalenses for far-field super-resolution imaging. Nat Commun 2012;3:1205.
[18] Rho J, Ye Y, Xiong Y, et al. Spherical hyperlens for two-dimensional sub-diffractional imaging at visible frequencies. Nat Commun 2010;1:143.
[19] Smith EJ, Liu Z, Mei YF, Schmidt OG. System investigation of a rolled-up metamaterial optical hyperlens structure. Appl Phys Lett 2009;95:083104.
[20] Xiong Y, Liu Z, Zhang X. Projecting deep-subwavelength patterns from diffraction-limited masks using metal-dielectric multilayers. Appl Phys Lett 2008;93:111116.
[21] Xiong Y, Liu Z, Zhang X. A simple design of flat hyperlens for lithography and imaging with half-pitch resolution down to 20 nm. Appl Phys Lett 2009;94: 203108.
[22] Wan W, Ponsetto JL, Liu Z. Numerical study of hyperlenses for three-dimensional imaging and lithography. Opt Express 2015;23:18501–10.
[23] Kildishev AV, Chettiar UK, Jacob Z, Shalaev VM, Narimanov E. Materializing a binary hyperlens design. Appl Phys Lett 2009;94:071102.
[24] Yan K, Liu L, Liu KP, et al. Far-field super-resolution imaging of nano-transparent objects by hyperlens with plasmonic resonant cavity. Plasmonics 2016;11:475.
[25] Sun J, Shalaev MI, Litchinitser NM. Experimental demonstration of a non-resonant hyperlens in the visible spectral range. Nat Commun 2015;6:7201.
[26] Prokopeva LJ, Kildishev AV. Expanding the theory of circular omnidirectional light concentrators to elliptic and spheroidal designs. J Opt 2016;18:044014.
[27] Pendry JB, Schurig D, Smith DR. Controlling electromagnetic field. Science 2006;312:1780–2.
[28] Ni X, Liu Z, Kildishev AV. Photonics DB: Optical constants, 2008. (Accessed May 23, 2016, https://nanohub.org/resources/PhotonicsDB.)
[29] Johnson PB, Christy RW. Optical constants of the noble metals. Phys Rev B 1972;6:4370–9.
[30] Boyd RW. Nonlinear optics, 3rd ed. Academic Press, London, 2008.
[31] Oulton RF, Sorger VJ, Genov DA, Pile DFP, Zhang X. A hybrid plasmonic waveguide for subwavelength confinement and long-range propagation. Nat Photonics 2008;2:496–500.
[32] Nielsen MP, Lafone L, Rakovich A, et al. Adiabatic nanofocusing in hybrid gap plasmon waveguides on the silicon-on-insulator platform. Nano Lett 2016;16:1410–4.

Supplemental Material: The online version of this article offers supplementary material (https://doi.org/10.1515/nanoph-2017-0054).